Self-Consistent Analysis of High-Temperature Effects on Strained-Layer Multiquantum-Well InGaAsP–InP Lasers

Joachim Piprek, *Senior Member, IEEE*, Patrick Abraham, *Senior Member, IEEE*, and John E. Bowers, *Fellow, IEEE*

***Abstract*—We present a comprehensive evaluation of temperature effects on threshold current and slope efficiency of 1.55 μm Fabry–Perot ridge-waveguide lasers between 20 °C and 120 °C. Experimental results are analyzed using the commercial laser simulator PICS3D. The software self-consistently combines two-dimensional carrier transport, heat flux, strained quantum-well gain computation, and optical waveguiding with a longitudinal mode solver. All relevant physical mechanisms are considered, including their dependence on temperature and local carrier density. Careful adjustment of material parameters leads to an excellent agreement between simulation and measurements at all temperatures. At lower temperatures, Auger recombination controls the threshold current and the differential internal efficiency. At high temperatures, vertical electron leakage from the separate confinement layer mainly limits the laser performance. The increase of internal absorption is less important. However, all these carrier and photon loss enhancements with higher temperature are mainly triggered by the reduction of the optical gain due to wider Fermi spreading of electrons.**

***Index Terms*—Laser measurements, laser thermal factors, numerical analysis, optical losses, quantum-well devices, semiconductor device modeling, semiconductor lasers, temperature.**

I. Introduction

THE PERFORMANCE of long-wavelength (1.3 or 1.55 μm) InGaAsP–InP laser diodes is known to be strongly temperature-dependent [1]. Self-heating or ambient temperature elevation cause the threshold current to increase and the slope efficiency to decrease. During the last two decades, much effort has been devoted to the explanation and the reduction of the temperature sensitivity of long-wavelength lasers [1], [2]. CW lasing has been achieved up to 165 °C (1.55 μm) [3] and 160 °C (1.3 μm) [4], respectively. AlGaInAs–InP lasers have shown CW operation up to 170 °C as well as a record-high lasing temperature of 210 °C in pulsed operation (1.3 μm) [5]. The difference between both temperatures reflects the effect of self-heating. It is larger for 1.3-μm AlGaInAs–InGaAs lasers (CW: 155 °C, pulsed: 210 °C), which is mainly due to the smaller thermal conductivity of the InGaAs substrate [6]. However, the physical mechanisms dominating the temperature sensitivity are still under discussion. In recent years, this discussion includes Auger recombination [7], intervalence band absorption (IVBA) [8], thermionic carrier emission out of the active region [9], lateral carrier spreading [10], passive layer absorption [11], spontaneous recombination within passive layers [12], and optical gain reductions [13], [14]. Combinations of several effects need to be considered to explain experimental results [15]. Different physical mechanisms govern in different temperature regions with a critical transition temperature [16]. Gain and loss mechanisms depend on the distribution of electrons and holes [17]. One-sided models can lead to one-sided interpretations of experiments and can contribute to the controversy in this field. In this paper, we present an analysis of measurements considering all of the above physical mechanisms and their interaction self-consistently.

Sophisticated numerical laser models have been developed by several research groups and advanced commercial software is available to the public. Some of these models have been used to study temperature effects on GaAs-based lasers [18], [19]. CW lasing of 1.3-μm InGaAsP–InP buried-heterostructure lasers was simulated using two-dimensional (2-D) models which include the internal heat flux [10], [20]. The more comprehensive these models are, the more material parameters are involved. Accurate data for material parameters of ternary and quaternary semiconductor compounds are not always available [21]. The composition of active region materials is often not exactly known [22]. Some parameters may depend on the growth conditions. Thus, careful adjustment of material parameters used in the model is required to find agreement with measurements. Simultaneous reproduction of several experimental results is often necessary to analyze the relative importance of different mechanisms. For example, agreement with the measured threshold current is obtained by fitting the Auger recombination parameter or by fitting the absorption coefficient. The correct balance between both mechanisms can be found by simultaneous reproduction of the measured slope efficiency. The number of uncertain material parameters should be kept as small as possible by simplifying the experimental situation simulated. Pulsed laser operation at different stage temperatures, for instance, can be used to avoid self-heating of the device and to exclude heat flux from the model. Thermal conductivity parameters in heterostructures are often not exactly known [23], leading to the risk of inaccurate active region temperatures in CW simulations. Sophisticated laser simulation tools are available today but a comprehensive agreement with measurements is seldom achieved. However, only the reproduction of a variety of experimental results gives the confidence that relevant physical effects are incorporated

Manuscript received May 6, 1999; revised November 4, 1999. This work was supported by the Center for Multidisciplinary Optical Switching Technology (MOST) a DARPA-sponsored MURI (Multidisciplinary Research Initiative).

The authors are with the Department of Electrical and Computer Engineering, University of California at Santa Barbara, Santa Barbara, CA USA 93106.

Publisher Item Identifier S 0018-9197(00)01807-8.

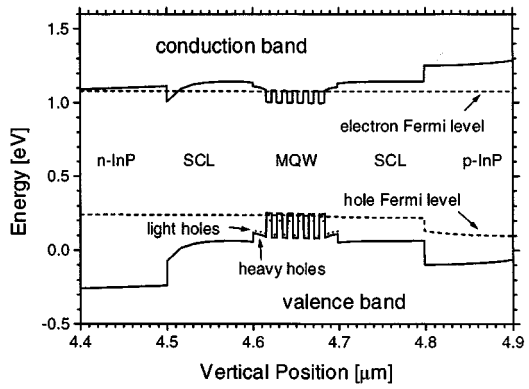

Fig. 1. Energy band diagram of the InGaAsP–InP waveguide region at threshold ($T = 20$ °C).

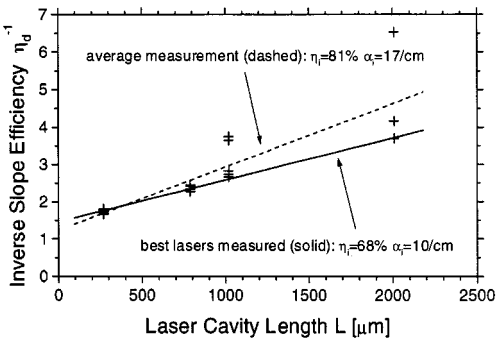

Fig. 2. Extraction of internal differential efficiency η_i and internal optical loss α_i from the measured slope efficiencies (+).

correctly in the model. Such an analysis is presented here using the commercial laser diode simulator PICS3D.[1] It includes the nonuniformity of the multiquantum-well (MQW) carrier distribution which was recently found to strongly affect the differential internal efficiency of 1.55-μm MQW lasers at room temperature [17].

We measure and analyze the high-temperature performance of broad-area Fabry–Perot InGaAsP–InP ridge-waveguide laser diodes emitting at the 1.55-μm wavelength. The MQW active region contains six compressively strained wells. Threshold current, slope efficiency at threshold, lasing wavelength, internal absorption loss, and differential internal efficiency are measured within the temperature range of 20 °C–120 °C. Section II describes the device structure and experimental results. Physical models and key material parameters are discussed in Section III. The results of our numerical analysis are presented in Section IV.

II. Device Structure and Experimental Results

The laser structures are grown in a metalorganic vapor phase epitaxy (MOVPE) horizontal reactor at 645 °C and 350 torr. The MQW energy band diagram is given in Fig. 1. The active region consists of six 6.4-nm-thick compressively strained (1%) $In_{0.76}Ga_{0.24}As_{0.79}P_{0.21}$ quantum wells (QW's). The 5.5-nm-thick barriers are made of $In_{0.71}Ga_{0.29}As_{0.55}P_{0.45}$ (1.25-μm bandgap wavelength) and exhibit slight tensile strain (0.04%). The first and the last barriers are 17 nm wide. The MQW stack is sandwiched between undoped 100-nm-thick 1.15-μm InGaAsP separate confinement layers (SCL's). On the p-side of the structure, the first 140 nm of the 2000-nm InP cladding layer next to the SCL are not intentionally doped. The remainder of the InP layer is 4×10^{17} cm^{-3} Zn doped. This low doping density reduces absorption losses and prevents Zn dopants from diffusing significantly toward the active region [24]. Zn atoms from our 3×10^{19} cm^{-3} doped 150-nm-thick InGaAs top contact layer are also not expected to diffuse into the active region [25]. We keep the Zn concentration at the SCL–InP interface negligibly low since its effect on electron leakage would add more uncertainty to our analysis [15], [26]. Broad-area ridge-waveguide lasers with 57-μm-wide stripes are processed. The p-ridge is etched down to the SCL layer. The lasers are characterized as cleaved. Lasers with different cavity lengths from $L = 269$ μm to 2008 μm are manufactured.

At room temperature, the lasing wavelength is $\lambda = 1536$ nm. Light power versus current (L–I) curves are measured under pulsed conditions (0.05% duty cycle) to avoid self-heating. A threshold current of $I_{\rm th} = 114$ mA, a threshold current density of $j_{\rm th} = 743$ A/cm^2, and a total slope efficiency of $\eta_d = 0.57$ are measured with $L = 269$ μm. The threshold voltage is $V_{\rm th} = 1.2$ V and the current–voltage (I–V) characteristic is linear above threshold (up to 260 mA) with $dV/dI = 2.4$ Ω. The latter number represents the series resistance of the laser, giving a 0.27-V voltage drop at threshold. Other contributions to the threshold voltage can be extracted from Fig. 1 which shows a 0.84-V Fermi level separation in the MQW and 0.09 V excess voltage at the p-side SCL–InP interface. All three numbers add up to the measured threshold voltage. Any significant Zn concentration at our p-side SCL–InP interface would strongly reduce the excess voltage and it would increase the electron barrier. High excess voltage has been associated with significant electron leakage in 1.3-μm lasers [27]. However, at room temperature, electron leakage in 1.3-μm lasers with an undoped InP–SCL interface is negligible near threshold and is significant only at very high injection currents [26]. Similarly, we previously found high-injection leakage in our 1.55-μm lasers [17]. In this paper, we investigate laser performance near threshold and we expect negligible electron leakage *at room temperature*, as suggested by our I–V linearity [27].

The inverse slope efficiency η_d^{-1} is plotted versus cavity length L to extract the internal optical loss α_i and the differential internal efficiency η_i (Fig. 2). The data points are expected to form a straight line [28], but significant scattering is often observed. This scattering is attributed to microstructural differences as well as to nonuniform current injection with long cavity lengths. We used up to three probes to make the current injection more homogeneous. The average facet power reflectivity is assumed to be $R = 0.28$. If all data points are taken into account, the standard deviation of both the extracted parameters is quite large: $\alpha_i = 17$/cm $\pm$ 6/cm and $\eta_i = 0.81 \pm 0.14$. Selecting only the best lasers with the lowest threshold current and the highest slope efficiency gives more narrow margins: $\alpha_i = 10$/cm $\pm$ 1/cm and $\eta_i = 0.68 \pm 0.02$. Besides statistical deviations, the $\eta_d^{-1}(L)$ method also exhibits an inherent inaccuracy since the length dependence of α_i and

[1]PICS3D 4.1.2 by Crosslight Software, 1998.

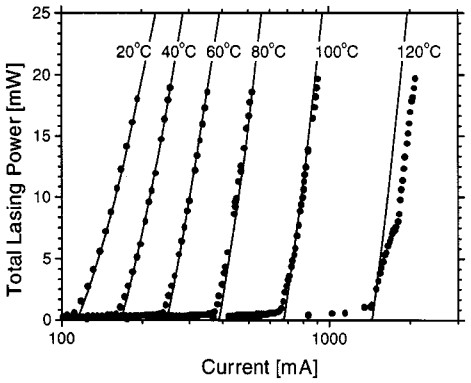

Fig. 3. Pulsed laser power versus current (L–I) characteristics at various temperatures (dots: measurement; lines: simulation).

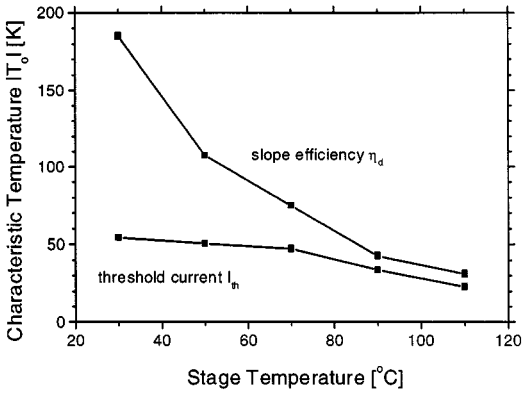

Fig. 4. Characteristic temperatures measured as a function of stage temperature.

η_i is neglected. For our short lasers ($L = 269$ μm), the inherent error of the differential internal efficiency is only a few percent whereas the internal optical loss is underestimated by about 30% [29]. For those reasons, we mainly rely on the directly measured laser parameters $I_{\rm th}(T)$ and $\eta_d(T)$ to investigate temperature effects. We use a typical short-cavity laser in the following.

The device temperature is increased by heating the copper stage from room temperature (20 °C) up to 120 °C. The thermal red-shift of the emission wavelength is $d\lambda/dT = -0.54$ nm/K. This red-shift is governed by the shift of the gain peak and is about twice as strong as in GaAs-based Fabry–Perot lasers [19]. Temperature effects on our pulsed L–I characteristics are shown in Fig. 3 (note the log scale). The effect of temperature elevation from T_1 to T_2 on the threshold current $I_{\rm th}(T)$ is often described by a characteristic temperature $T_o = (T_2 - T_1)/\ln[(I_{\rm th}(T_2)/I_{\rm th}(T_1)]$. Utilizing this concept, we obtain a function $T_o(T)$ which decreases from 55 K at room temperature to 20 K at 110 °C (Fig. 4). Similarly, the characteristic temperature of the slope efficiency $\eta_d(T)$ shows a monotonic change from −180 K to −30 K (Fig. 4). Thus, the temperature sensitivity of both the threshold current and the slope efficiency is strongly increasing with higher temperature. In the following, we analyze the physical mechanisms behind these temperature effects.

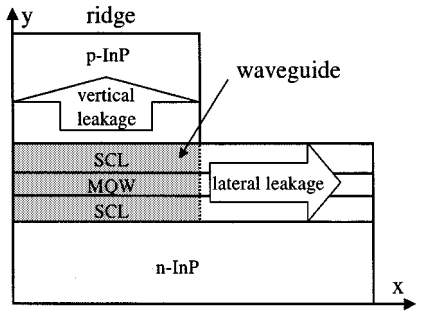

Fig. 5. Illustration of leakage currents from the waveguide region in the lateral (ambipolar) and vertical (electrons) directions.

III. Laser Models and Material Parameters

PICS3D self-consistently combines 2-D carrier transport, heat flux, optical gain computation, and waveguiding within the transversal plane (x, y) as well as a mode solver in the longitudinal direction (z). The laser is separated into many 2-D sections along the longitudinal axis, allowing for a quasi-3-D simulation. However, longitudinal variations are of minor importance in our device. Further details of the laser model are published elsewhere [30].[2] We discuss here only those aspects that are crucial to our analysis. By measuring pulsed laser characteristics, we are able to exclude self-heating effects which would add another level of uncertainty to the analysis. In our investigation, the temperature of the active region is equal to the stage temperature.

The drift-diffusion model of carrier transport includes Fermi statistics and thermionic emission at heterobarriers [31]. This process is mainly controlled by the offset of the conduction band (ΔE_c) and valence band (ΔE_v) at the heterobarrier. We find best agreement with the measurements by using a band offset ratio of $\Delta E_c/\Delta E_v = 0.4/0.6$ which is typical for the InGaAsP–InP system [32]. In our steady-state analysis, carrier scattering between confined and unconfined QW states is not considered explicitly. A single quasi-Fermi level is assumed and QW carriers are treated as 3-D within the transport equations. More sophisticated models are required to investigate dynamic laser characteristics [33]. Fig. 5 illustrates leakage currents in our device. Vertical leakage is due to electrons leaving the waveguide region in the vertical y direction by thermionic emission. We draw the boundary along the SCL–InP interface in order to clearly separate electron leakage from other physical mechanisms. Vertical hole leakage into n-InP is also part of the model but it is negligible. Lateral leakage includes all carriers leaving the waveguide region in the lateral x direction. Both the leakage currents plus all recombination currents within the active (QW) and passive layers of the waveguide region add up to the injection current I. Within passive layers, a temperature-independent spontaneous emission parameter of $B = 10^{-10}$ cm$^3 \cdot$ s^{-1} is assumed. The spontaneous recombination rate in QW's is much larger than in passive layers and is calculated self-consistently from the energy band structure and Fermi distribution including temperature effects. A 2-D profile of spontaneous recombination in the MQW region is shown in

[2]PICS3D User's Manual. [Online]. Available http://www.crosslight.ca

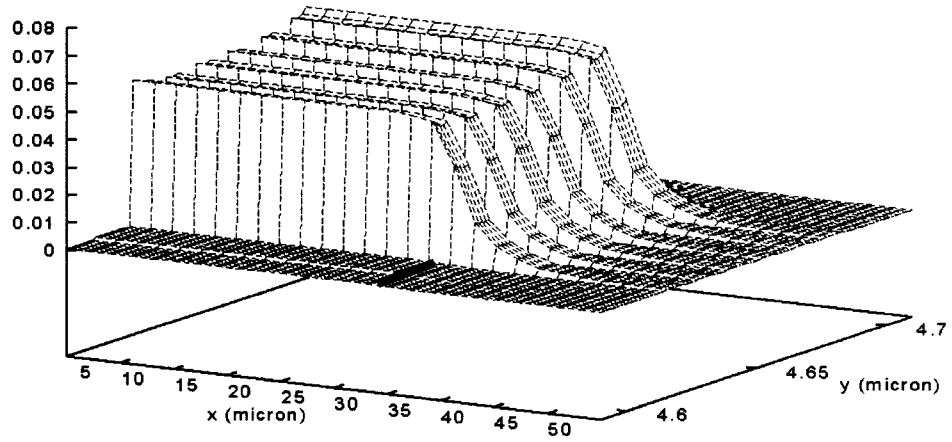

Fig. 6. Profile $R_{\rm spon}(x, y)$ of the spontaneous emission rate [10^{28} cm^{-3}s^{-1}] within the MQW region at 120°C. The upper (p-side) quantum well exhibits the strongest recombination. Emission beyond the ridge region ($x > 28.5$ μm = thick line) indicates lateral leakage.

Fig. 6 as calculated at $T = 120$ °C. QW recombination outside the ridge region ($x > 28.5$ μm) indicates lateral leakage. Using the total spontaneous recombination rate and the average carrier densities, an average QW parameter $B = 0.8 \times 10^{-10}$ cm$^3 \cdot$s^{-1} is estimated at 120 °C. It is smaller than the room-temperature value $B = 1.2 \times 10^{-10}$ cm$^3 \cdot$s^{-1}, as expected. Our relatively low room-temperature threshold current density indicates small nonradiative recombination. The Shockley–Read–Hall (SRH) recombination lifetime of electrons and holes is assumed to be 20 ns within the MQW stack and 100 ns elsewhere. Published measurements of the QW Auger recombination rate CN^3 versus the average QW carrier density N show a weak temperature dependence in strained-layer 1.55-μm MQW lasers [13], [34]. There is some uncertainty about the carrier density measurement [35]; however, the Auger parameter C is found to be hardly temperature-dependent. By definition, the experimental parameter C is somewhat different from the theoretical parameters C_n and C_p used in the calculations of the local Auger recombination rate $(C_n n + C_p p)(np - n_i^2)$ (n–electron density, p–hole density, n_i–intrinsic carrier density). Seki *et al.* have investigated this difference [36]. Assuming that the conduction-hole-hole-split-off (CHHS) Auger process dominates ($C_n = 0$), they reproduce the small temperature sensitivity of the experimental results employing an Arrhenius-type function for the parameter $C_p = C_o \exp(-E_a/kT)$ with an activation energy of $E_a = 60$ meV. We adopt this concept here using the same activation energy which gives good agreement with our measurements. Our fit leads to an Auger parameter of $C_p = 1.6 \times 10^{-28}$ cm$^6 \cdot$s^{-1} at room temperature which rises to 2.9×10^{-28} cm$^6 \cdot$s^{-1} at 120 °C.

In our strained QW's, the conduction bands are assumed to be parabolic and the nonparabolic valence bands are computed by the 4 × 4 kp method including valence band mixing [37]. The local optical gain is calculated self-consistently from the local Fermi distribution of carriers at each bias point of the L–I curve. A Lorentzian broadening function is used with 0.1 ps intraband relaxation time. Band gap shrinkage due to carrier-carrier interaction is considered as $\Delta E_g = -\xi N^{1/3}$ with $\xi = 10^{-8}$ eV cm. The thermal bandgap reduction parameter $dE_g/dT = -0.28$ meV/K is extracted from the measured thermal shift of the lasing wavelength. This number

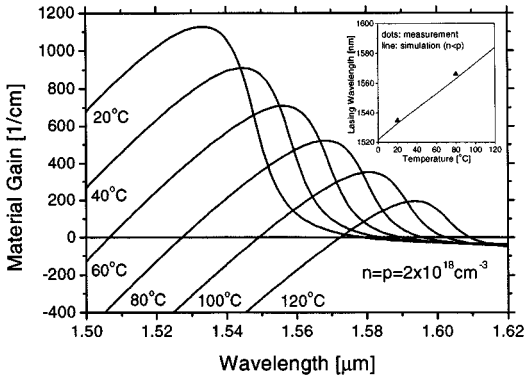

Fig. 7. Material gain spectrum for various temperatures (inset: shift of the lasing wavelength).

is in agreement with measurements of the photoluminescence peak shift of similar MQW's [22]. Temperature effects on the calculated gain spectrum are shown in Fig. 7 for a carrier density of $n = p = 2 \times 10^{18}$ cm^{-3}. With higher temperature, the peak gain decreases substantially due to the wider spreading of the Fermi distribution of carriers. The negative gain below the bandgap energy is a deficiency of the Lorentz broadening model [38], but it hardly affects our analysis. The inset shows the good agreement of the calculated lasing wavelength with measurements. Because of the temperature dependence of the carrier densities ($p > n$), it slightly deviates from the gain peak position shown. Fig. 8 plots the peak gain as a function of the carrier density at different temperatures. To maintain the required threshold gain with rising temperature, carrier density and injection current need to be increased. We will show in Section IV that this is the main trigger mechanism for the observed temperature sensitivity of the threshold current.

Several absorption mechanisms are considered in PICS3D. The local absorption coefficient is proportional to the density of electrons and holes: $\alpha = \alpha_b + k_n n + k_p p$. The constant background loss coefficient α_b represents carrier-density-independent mechanisms like photon scattering at defects. Free-carrier absorption due to electrons is known to be very small in 1.55-μm InGaAsP–InP lasers ($k_n = 10^{-18}$ cm^2) [2]. Absorption within the valence bands can be related to intraband transitions (free-carrier absorption) or to interband

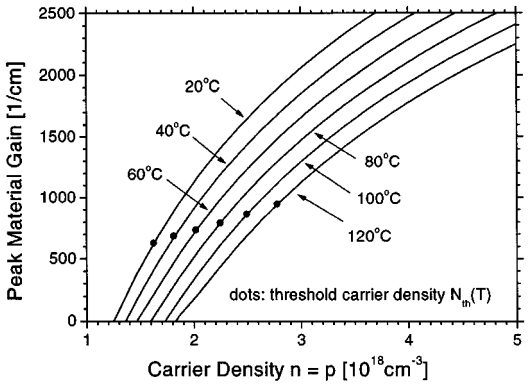

Fig. 8. Peak material gain versus carrier density ($n = p$) at different temperatures. Dots give the average QW carrier density at threshold as obtained from the simulation ($p > n$).

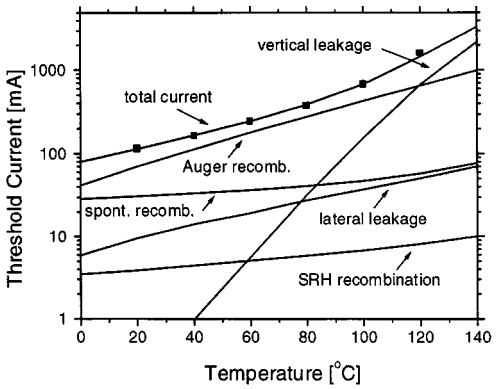

Fig. 9. Pulsed threshold current and its components (dots: measurements, lines: simulation).

transitions (IVBA). Both mechanisms are roughly proportional to the hole density and hard to separate in our analysis. IVBA is usually considered the dominant absorption mechanism in 1.55-μm lasers [2]. Absorption measurements at the 1.55-μm wavelength give $k_p = 20 \cdots 60 \times 10^{-18}$ cm^2 for bulk material (InGaAsP exhibits higher values than InP) [39]–[42]. It is difficult to accurately measure this parameter within QW's, and only a few experimental investigations of k_p can be found in the literature on 1.55-μm MQW structures [42], [43]. IVBA is often believed to be reduced by compressive strain, but some investigations suggest otherwise [44], [45]. QW IVBA is hard to distinguish from IVBA in other layers, and we assume k_p and k_n to be uniform throughout our device, i.e., carrier-density-dependent absorption within barriers and SCL's is included self-consistently. Our fit to L–I measurements gives $k_p = 82 \times 10^{-18}$ cm^2 at room temperature. This number mainly represents the QW's (cf. Section IV). It is smaller than measured with unstrained QW's (140×10^{-18} cm^2) and larger than with more strongly strained QW's (35×10^{-18} cm^2 with 1.2% strain) [42]. We find a very weak temperature sensitivity of this parameter ($k_p = 88 \times 10^{-18}$ cm^2 at 120 °C) which is in agreement with theoretical [46] and experimental [14], [39], [41], [47] results of other researchers. The modal internal loss parameter α_i is obtained by 3-D integration, weighted by the local intensity of the fundamental mode (optical confinement factor $\Gamma = 0.074$). Temperature effects on $\alpha_i(T)$ are mainly caused by the temperature-dependent carrier density. For our lasers, vanishing background loss ($\alpha_b = 0$) and $R = 0.28$ facet power reflectance give the best agreement with L–I measurements at a different laser length. The mirror loss coefficient is $\alpha_m = 47$ cm^{-1} for our cavity length of $L = 269$ μm.

By choosing the highest level of self-consistency in PICS3D, each bias point of our L–I simulation requires about 10 min of computation on a 500-MHz Pentium III computer, amounting to about 2 h for each L–I curve.

IV. Analysis of Experimental Results

The simulated L–I characteristics are given in Fig. 3 (lines) for device temperatures from 20 °C to 120 °C. The excellent agreement with the measurements is obtained by careful adjustment of key material parameters as discussed in Section III. The Auger coefficient C_p has the strongest influence on the calculated threshold current. Surprisingly, it also affects the slope efficiency (see below). The second most crucial fit parameter is the absorption parameter k_p. The band offset ratio $\Delta E_c/\Delta E_v$ only controls high-temperature L–I curves, indicating negligible vertical leakage at lower temperatures. The fit in Fig. 3 is mainly achieved by balancing these three material parameters.

Fig. 9 plots the threshold current and its components as a function of temperature. All recombination currents are obtained by 3-D integration over the waveguide region (Fig. 5). Carriers leaving the waveguide region in the lateral or vertical direction constitute leakage currents. At room temperature, the strongest contribution to the total threshold current comes from QW Auger recombination (61%), followed by spontaneous emission (27%), lateral leakage current (8%), and SRH recombination (3%). Vertical carrier leakage is negligible at 20 °C which is also indicated by the straight electron quasi-Fermi level at the p-side SCL–InP interface (Fig. 1). Relevant current flow across this undoped interface would be accompanied by a step in the quasi-Fermi level which is clearly visible in the case of holes. Hot carriers are not included in our simulation, i.e., carriers instantaneously assume a Fermi distribution. At 120 °C, vertical electron leakage into p-InP becomes the dominant carrier loss mechanism (47%), leaving behind Auger recombination (45%), spontaneous emission (4%), lateral leakage (3%), and SRH recombination (1%). All these calculated contributions add up perfectly to the measured threshold currents (dots in Fig. 9). Its temperature sensitivity is dominated by Auger recombination at lower temperatures and by vertical leakage at higher temperatures. A critical transition temperature T_c can be defined by the beginning dominance of vertical leakage current (120 °C) or by the drop of the characteristic temperature near 80 °C (cf. Fig. 4). The second definition is less precise but more suitable from an experimental point of view. Below $T_c = 80$ °C, the characteristic temperatures of Auger current (44 K) and spontaneous recombination current (217 K) are close to the numbers found by other authors [7]. At higher temperatures, T_o of the spontaneous recombination drops to 80 K, indicating the increasing contribution from carriers in passive layers. Characteristic temperatures for vertical leakage, lateral leakage, and SRH recombination are about 14, 62, and 127 K, respectively.

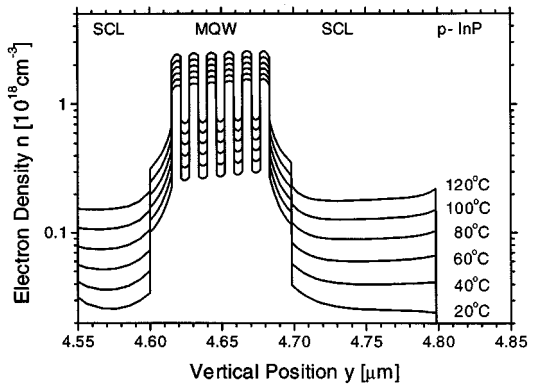

Fig. 10. Threshold electron density $n(y)$ at the laser axis for different temperatures.

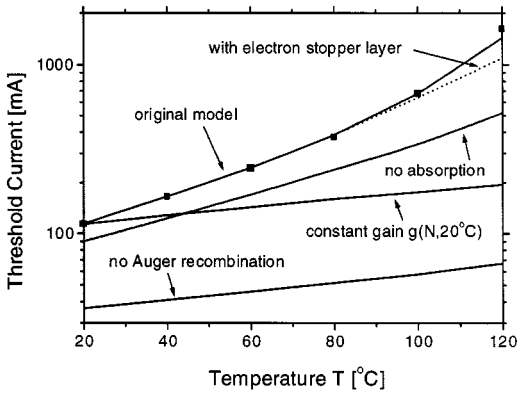

Fig. 11. Simulated threshold current for different variations of the model (dots—measurement).

All these carrier loss mechanisms depend on the carrier distribution (Fig. 10). From 20 °C to 120 °C, the average QW carrier density N increases from 1.6×10^{18} cm^{-3} to 2.8×10^{18} cm^{-3}. The enhancement of carrier density and carrier losses is mainly triggered by the gain reduction with higher temperature. This becomes clear from Fig. 11 which shows a threshold current simulation assuming $T = 20$ °C in all gain calculations. Without temperature effects on the gain, the temperature sensitivity of the threshold current is very small ($T_o = 188$ K), despite Auger recombination. This result confirms experimental investigations by other authors [13], [14] which have been disputed elsewhere [7].

The maximum lasing temperature of our devices is limited by vertical electron leakage into the InP ridge. From 20 °C to 120 °C, the electron density at the p-side SCL–InP interface rises by more than one order of magnitude (Fig. 10). This is accompanied by an elevation of the electron quasi-Fermi level on the SCL side (F_n^{SCL}). Both its reduced distance to the InP conduction band edge E_c^{InP} and the increased temperature lead to the escalation of the thermionic emission current density across this interface [31]

$$j_n^{leak} = AT^2\left[\exp\left(\frac{F_n^{\mathrm{InP}} - E_c^{\mathrm{InP}}}{kT}\right) - \exp\left(\frac{F_n^{\mathrm{SCL}} - E_c^{\mathrm{InP}}}{kT}\right)\right]. \quad (1)$$

where

- A effective Richardson constant;
- k Boltzmann constant;
- F_n^{InP} electron quasi-Fermi level on the InP side of the interface.

Most of the leaking electrons drift toward the contact, and the p-InP minority carrier density rises from 10^{13} cm^{-3} at 20 °C to 5×10^{15} cm^{-3} at 120 °C. We have recently reported on the introduction of an InGaP layer at the p-side SCL–InP interface to heighten the energy barrier for electrons [48]. The effect of this electron stopper layer is illustrated by the dotted line in Fig. 11. It has no effect at lower temperatures but it reduces the threshold current at high temperatures. Consistent with this analysis, the introduction of a p-AlInAs electron stopper layer into 1.3-μm AlGaInAs–InP lasers led to the record-high lasing temperature of 210 °C [5]. The vertical electron leakage current can also be reduced by p-doping of the SCL–InP interface [15], [26], [49].

From 20 °C to 120 °C, the Auger current rises tenfold which is mainly related to the 75% increase of the carrier density N ($p/n \sim 1.25$ in the QW's). The Auger coefficient $C_p(T)$ rises by less than a factor of 2. Fig. 11 gives the threshold current as calculated without Auger recombination ($C_p = C_n = 0$). This result is lower than the simple subtraction of the Auger current from the threshold current, especially at high temperatures (cf. Fig. 9). The corresponding slope efficiency is higher than with Auger recombination. This phenomenon is due to the smaller threshold voltage which gives reduced vertical leakage since MQW carrier nonuniformity and electron overflow into the p-side SCL are reduced [17] and the electron quasi-Fermi level at the p-side SCL–InP interface is lowered. Caused by this combination of effects, the characteristic temperature of the threshold current is $T_o = 173$ K when Auger recombination is removed from the model.

Thus far, we have analyzed temperature effects on the threshold current. More information about internal laser physics can be extracted from the measured slope efficiency $\eta_d(T)$ which is reproduced by our simulation (Fig. 12). The differential quantum efficiency $\eta_d = \eta_i\alpha_m/(\alpha_m + \alpha_i)$ is affected by internal optical losses (α_i) and by the enhancement of carrier losses above threshold (η_i). The differential internal efficiency $\eta_i = \Delta I_{stim}/\Delta I$ is the fraction of the total current increment ΔI above threshold that results in the stimulated emission of photons [38]. It is less than unity if parts of ΔI are consumed by other recombination processes (Auger recombination, spontaneous recombination, and SRH recombination; current increment ΔI_r) or by leakage (vertical leakage increment ΔI_e, lateral leakage increment ΔI_s) [50]. The total current increment is the sum of all these contributions: $\Delta I = \Delta I_{\mathrm{stim}} + \Delta I_r + \Delta I_e + \Delta I_s$. The corresponding differential efficiencies are given as

$$\eta_i = \eta_s \times \eta_e \times \eta_r = \frac{\Delta I_{\mathrm{stim}} + \Delta I_r + \Delta I_e}{\Delta I_{\mathrm{stim}} + \Delta I_r + \Delta I_e + \Delta I_s} \times \frac{\Delta I_{\mathrm{stim}} + \Delta I_r}{\Delta I_{\mathrm{stim}} + \Delta I_r + \Delta I_e} \times \frac{\Delta I_{\mathrm{stim}}}{\Delta I_{\mathrm{stim}} + \Delta I_r}. \quad (2)$$

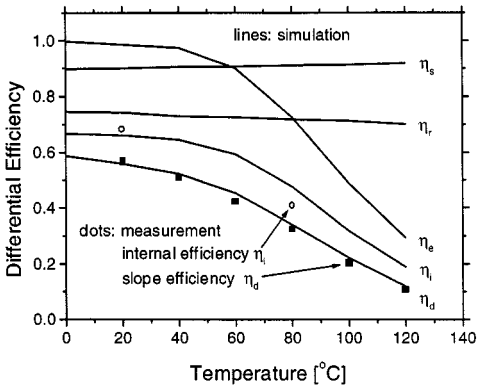

Fig. 12. Differential efficiencies versus temperature (dots: measurement; lines: simulation). The internal efficiency $\eta_i = \eta_e\eta_r\eta_s$ is separated into contributions from vertical leakage (η_e), lateral leakage (η_s), and recombination losses (η_r).

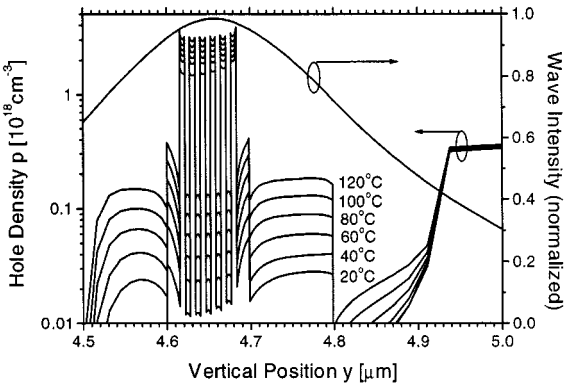

Fig. 13. Threshold hole density $p(y)$ and wave intensity at the laser axis with the stage temperature as the parameter.

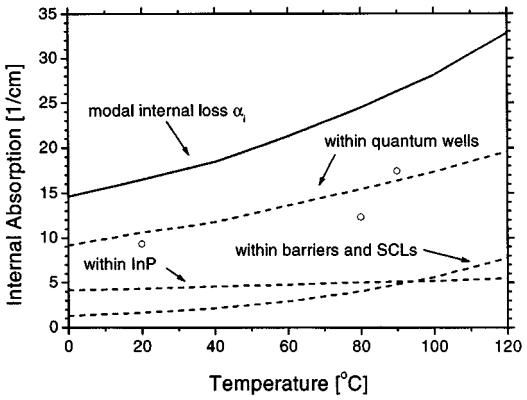

Fig. 14. Internal optical loss of the fundamental mode. Dashed lines give contributions of different device regions. Dots give α_i as extracted from L–I curves (cf. Fig. 2).

These efficiencies can also be understood as probabilities. An additional electron injected above threshold has the probability η_s to remain within the ridge region ($x < 28.5$ μm). It has the probability $\eta_s\eta_e$ to recombine within the waveguide region. The efficiency η_r gives the ratio of the stimulated recombination increment to the total recombination increment within the waveguide region (including MQW). The difference between both the recombination rates is considered recombination loss. The recombination loss within SCL's and barriers is more than one order of magnitude smaller than within the QW's (cf. Fig. 6).

We have recently shown that QW recombination losses dominate the differential internal efficiency of our MQW lasers at room temperature [17]. Their commonly neglected influence is based on the increasing nonuniformity of the QW carrier population with higher current. The separation of quasi-Fermi levels in neighboring QW's increases with higher current due to the electrical resistance of the barrier. This causes an increment of Auger recombination within the more populated p-side QW's that is larger than the decrement in the less populated n-side QW's. The net increase of Auger recombination above threshold dominates η_i at room temperature [17]. Lateral leakage has a much smaller influence and vertical leakage is negligible at lower temperatures (Fig. 12).

Again, this ranking changes dramatically at high temperatures. Above 80 °C, electron leakage causes the highest differential carrier loss. The recombination loss increment ΔI_r rises little with higher temperature. This is related to the more uniform hole distribution (Fig. 13) which compensates for rising Auger recombination. Due to a lower carrier mobility, the lateral leakage increment ΔI_s decreases slightly, thereby reducing the temperature sensitivity of the slope efficiency [51]. The critical temperature $T_c = 80$ °C of $\eta_d(T)$ is identical to the one extracted from the temperature sensitivity of the threshold current. However, T_c is difficult to identify from the measured change of the characteristic temperature of $\eta_d(T)$, as proposed by other authors [16]. In fact, the strongest change in Fig. 4 occurs near 40 °C, when the efficiency $\eta_d(T)$ starts to drop (Fig. 12). The open circles in Fig. 12 give experimental results for the internal efficiency η_i as obtained by the $\eta_d^{-1}(L)$ method, which confirm our simulation (cf. Section II).

Finally, we analyze temperature effects on the modal optical loss $\alpha_i(T)$. Absorption is governed by the density of holes which is the highest in the QW's (Fig. 13). At room temperature, 64% of the internal optical loss occurs within the QW's and 10% within barriers and SCL's (Fig. 14). The remaining 26% originate in the p-InP cladding layer which is occupied by a considerable part of the guided wave (Fig. 13). At 120 °C, the QW's cause 60% of the internal absorption whereas the contribution of barriers and SCL's rises to 24%. The total absorption doubles within this temperature range. As suggested by other authors [11], [16], absorption by unconfined carriers rises strongly with temperature elevation. However, passive layer absorption does not dominate internal optical losses in our lasers. Fig. 14 also gives experimental results for α_i obtained by the $\eta_d^{-1}(L)$ method which show some scattering and which are all smaller than calculated. This disagreement is an inherent problem of the $\eta_d^{-1}(L)$ method with short lasers and it does not invalidate our simulation [29].

Photon losses have less effect on the slope efficiency η_d than carrier losses. From 20 °C to 120 °C, the optical efficiency $\alpha_m/(\alpha_m + \alpha_i)$ decreases from 0.74 to 0.56 while the differential internal efficiency η_i drops from 0.66 to 0.19, mainly due to vertical leakage (Fig. 12). Below the critical temperature of 80 °C, the effect of absorption on the threshold current's temperature sensitivity is also small. When we exclude absorption from the simulation, the constant mirror loss gives a

constant threshold gain and a smaller increase of the threshold carrier density with temperature (cf. Fig. 8). The characteristic temperature of the threshold current is slightly increased to 58 K (Fig. 11). However, the threshold current at 120 °C is almost three times smaller without absorption, mainly due to reduced vertical leakage.

V. Summary

Based on various light versus current measurements on 1.55-μm Fabry–Perot laser diodes, we have investigated the relative importance and the interaction of key physical mechanisms which are known to affect the temperature sensitivity of long-wavelength lasers. In our MQW laser, threshold current and slope efficiency are mainly governed by Auger recombination at low temperatures and by vertical electron leakage at high temperatures. The critical transition temperature is about 80 °C. The enhancement of carrier losses and internal absorption with rising temperature is mainly controlled by the increasing carrier density in active and passive layers. This increase is caused by optical gain reductions with higher temperature. Thus, only the self-consistent consideration of temperature effects on gain, carrier density, recombination, leakage, and absorption leads to a full explanation of the measured temperature sensitivity. Other types of laser diodes may exhibit a different balance of these mechanisms. A larger variety of experiments allows for the fine-tuning of more material parameters in the model. However, we have given an example of how advanced numerical models can extract detailed physical information from laser measurements and help to deepen the understanding of temperature effects.

References

[1] G. P. Agrawal and N. K. Dutta, *Semiconductor Lasers*. New York: Van Nostrand Reinhold, 1993.

[2] *Handbook of Semiconductor Lasers and Photonic Integrated Circuits*, Y. Suematsu and A. R. Adams, Eds., Chapman & Hall, London, U.K., 1994.

[3] M. Aoki, M. Komori, T. Tsuchiya, H. Sato, K. Nakahara, and K. Uomi, "InP-based reversed-mesa ridge-waveguide structure for high-performance long-wavelength laser diodes," *IEEE J. Select. Topics Quantum Electron.*, vol. 3, pp. 672–683, 1997.

[4] H. Oohashi, S. Seki, T. Hirono, H. Sugiura, T. Amano, M. Ueki, J. Nakano, M. Yamamoto, Y. Tohmori, M. Fukuda, and K. Yokoyama, "High-power and high-efficiency 1.3 μm InAsP compressively strained MQW lasers at high temperatures," *Electron. Lett.*, vol. 31, pp. 556–557, 1995.

[5] K. Takemasa, T. Munakata, M. Kobayashi, H. Wada, and T. Kamijoh, "High-temperature operation of 1.3 μm AlGaInAs strained multiple quantum well lasers," *Electron. Lett.*, vol. 34, pp. 1231–1233, 1998.

[6] K. Otsubo, H. Shoji, T. Kusunoki, T. Suzuki, T. Uchida, Y. Nishijima, K. Nakajima, and H. Ishikawa, "Long-wavelength strained quantum-well lasers oscillating up to 210 °C on InGaAs ternary substrates," *IEEE Photon. Technol. Lett.*, vol. 10, pp. 1073–1075, 1998.

[7] J. Braithwaite, M. Silver, V. A. Wilkinson, E. P. O'Reilly, and A. R. Adams, "Role of radiative and nonradiative processes on the temperature sensitivity of strained and unstrained 1.5μm InGaAs(P) quantum well lasers," *Appl. Phys. Lett.*, vol. 67, pp. 3546–3548, 1995.

[8] J. Piprek, D. Babic, and J. E. Bowers, "Simulation and analysis of double-fused 1.55μm vertical-cavity lasers," *J. Appl. Phys.*, vol. 81, pp. 3382–3390, 1997.

[9] L. J. P. Ketelsen and R. F. Kazarinov, "Carrier loss in InGaAsP-InP lasers grown by hydride CVD," *IEEE J. Quantum Electron.*, vol. 34, pp. 811–813, 1995.

[10] Y. Yoshida, H. Watanabe, K. Shibata, A. Takemoto, and H. Higuchi, "Analysis of characteristic temperature for InGaAsP BH lasers with p-n-p-n blocking layers using two-dimensional device simulator," *IEEE J. Quantum Electron.*, vol. 34, pp. 1257–1262, 1998.

[11] V. Mikhaelashvili, N. Tessler, R. Nagar, G. Eisenstein, A. G. Dentai, S. Chandrasakhar, and C. H. Joyner, "Temperature dependent loss and overflow effects in quantum well lasers," *IEEE Photon. Technol. Lett.*, vol. 6, pp. 1293–1296, 1994.

[12] A. A. Bernussi, H. Temkin, D. L. Coblentz, and R. A. Logan, "Effect of barrier recombination on the high temperature performance of quaternary multiquantum well lasers," *Appl. Phys. Lett.*, vol. 66, pp. 67–69, 1995.

[13] Y. Zou, J. S. Osinski, P. Grodzinski, P. D. Dapkus, W. C. Rideout, W. F. Sharfin, J. Schlafer, and F. D. Crawford, "Experimental study of Auger recombination, gain, and temperature sensitivity of 1.5μm compressively strained semiconductor lasers," *IEEE J. Quantum Electron.*, vol. 29, pp. 1565–1575, 1993.

[14] D. A. Ackerman, G. E. Shtengel, M. S. Hybertsen, P. A. Morgan, R. F. Kazarinov, T. Tanbun-Ek, and R. A. Logan, "Analysis of gain in determining T_0 in 1.3μm semiconductor lasers," *IEEE J. Select. Topics Quantum Electron.*, vol. 1, pp. 250–262, 1995.

[15] G. L. Belenky, C. L. Reynolds, D. V. Donetsky, G. E. Shtengel, M. S. Hybertsen, M. A. Alam, G. A. Baraff, R. K. Smith, R. F. Kazarinov, J. Winn, and L. E. Smith, "Role of p-doping profile and regrowth on the static characteristics of 1.3μm MQW InGaAsP-InP lasers: Experiment and modeling," *IEEE J. Quantum Electron.*, vol. 35, pp. 1515–1520, 1999.

[16] S. Seki, H. Oohashi, H. Sugiura, T. Hirono, and K. Yokoyama, "Study on the dominant mechanisms for the temperature sensitivity of threshold current in 1.3-μm InP-based strained-layer quantum-well lasers," *IEEE J. Quantum Electron.*, vol. 32, pp. 1478–1486, 1996.

[17] J. Piprek, P. Abraham, and J. E. Bowers, "Carrier nonuniformity effects on the internal efficiency of multiquantum-well lasers," *Appl. Phys. Lett.*, vol. 74, pp. 489–491, 1999.

[18] D. L. Foulger, P. M. Smowton, P. Blood, and P. A. Mawby, "Self-consistent simulation of (AlGa)InP/GaInP visible lasers," *Proc. Inst. Elect. Eng.*, vol. 144, pp. 23–29, 1997.

[19] U. Menzel, A. Barwolff, P. Enders, D. Ackermann, R. Puchert, and M. Voss, "Modeling the temperature dependence of threshold current, external differential efficiency and lasing wavelength in QW laser diodes," *Semicond. Sci. Technol.*, vol. 10, pp. 1382–1392, 1995.

[20] M. Gault, P. Mawby, A. R. Adams, and M. Towers, "Two-dimensional simulation of constricted-mesa InGaAsP/InP buried-heterostructure lasers," *IEEE J. Quantum Electron.*, vol. 30, pp. 1691–1700, 1994.

[21] S. Adachi, *Physical Properties of III-V Semiconductor Compounds*, New York: Wiley, 1992.

[22] S. Rapp, J. Piprek, K. Streubel, J. Andre, and J. Wallin, "Temperature sensitivity of 1.54 μm vertical-cavity lasers with an InP-Based bragg reflector," *IEEE J. Quantum Electron.*, vol. 33, pp. 1839–1845, 1997.

[23] J. Piprek, T. Troeger, B. Schroeter, J. Kolodzey, and C. S. Ih, "Thermal conductivity reduction in GaAs-AlAs distributed Bragg reflectors," *IEEE Photon. Technol. Lett.*, vol. 10, pp. 81–83, 1998.

[24] C. Blaauw, F. R. Shepherd, and D. Eger, "Secondary ion mass spectrometry and electrical characterization of Zn diffusion in n-InP," *J. Appl. Phys.*, vol. 66, pp. 605–610, 1989.

[25] V. Swaminathan, C. L. Reynolds, and M. Geva, "1.3μm InGaAsP/InP capped mesa buried heterostructure laser with an undoped cladding layer in base epitaxial growth," *J. Appl. Phys.*, vol. 83, pp. 4540–4541, 1998.

[26] G. L. Belenky, C. L. Reynolds, R. F. Kazarinov, V. Swaminathan, S. L. Luryi, and J. Lopata, "Effect of p-doping profile performance of strained InGaAsP-InP lasers," *IEEE J. Quantum Electron.*, vol. 32, pp. 1450–1455, 1996.

[27] E. J. Flynn and D. A. Ackerman, "Electron leakage and the excess voltage at p-P heterojunctions in InGaAsP/InP lasers," in *Int. Electr. Dev. Meeting, Tech. Dig.*, Washington, DC, , 1997, pp. 389–390.

[28] H. Kressel and J. K. Butler, *Semiconductor Lasers and Heterojunction LEDs*, New York: Academic, 1977.

[29] J. Piprek, P. Abraham, and J. E. Bowers, "Cavity length effects on internal loss and quantum efficiency of multi-quantum-well lasers," *IEEE J. Select. Topics Quantum Electron.*, vol. 5, pp. 643–647, 1999.

[30] Z.-M. Li, "Physical models and numerical simulation of modern semiconductor lasers," *Proc. SPIE*, vol. 2994, pp. 698–708, 1997.

[31] W. R. Frensley, "Heterostructure and quantum well physics," in *Heterostructures and Quantum Devices*, N. G. Einspruch and W. R. Frensley, Eds. San Diego, CA: Academic, 1994.

[32] S. L. Chuang, *Physics of Optoelectronic Devices*, New York: Wiley, 1995.

[33] M. Grupen and K. Hess, "Simulation of carrier transport and nonlinearities in quantum-well laser diodes," *IEEE J. Quantum Electron.*, vol. 34, pp. 120–140, 1998.
[34] G. Fuchs, C. Schiedel, A. Hangleiter, V. Haerle, and F. Scholz, "Auger recombination in strained and unstrained InGaAs/InGaAsP multi-quantum-well lasers," *Appl. Phys. Lett.*, vol. 62, pp. 396–398, 1993.
[35] G. E. Shtengel, D. A. Ackerman, P. A. Morton, E. J. Flynn, and M. S. Hybertsen, "Impedance-corrected carrier lifetime measurements in semiconductor lasers," *Appl. Phys. Lett.*, vol. 67, pp. 1506–1508, 1995.
[36] S. Seki, W. W. Lui, and K. Yokoyama, "Explanation for the temperature insensitivity of the Auger recombination rates in 1.55μm InP-based strained-layer quantum-well lasers," *Appl. Phys. Lett.*, vol. 66, pp. 3093–3095, 1995.
[37] S. L. Chuang, "Efficient band structure calculations of strained quantum wells," *Phys. Rev. B*, vol. 43, pp. 9649–9661, 1991.
[38] L. A. Coldren and S. W. Corzine, *Diode Lasers and Photonic Integrated Circuits*, New York: Wiley, 1995.
[39] H. C. Casey and P. L. Panish, "Variation of intervalence band absorption with hole concentration in p-type InP," *Appl. Phys. Lett.*, vol. 44, pp. 82–83, 1984.
[40] A. R. Adams, M. Asada, Y. Suematsu, and S. Arai, "The temperature dependence of the efficiency and threshold current of InGaAsP lasers related to intervalence band absorption," *Jap. J. Appl. Phys.*, vol. 19, pp. L621–L624, 1980.
[41] C. H. Henry, R. A. Logan, F. R. Merritt, and J. P. Luongo, "The effect of intervalence band absorption on the thermal behavior of InGaAsP lasers," *IEEE J. Quantum Electron.*, vol. QE-19, pp. 947–952, 1983.
[42] I. Joindot and J. L. Beylat, "Intervalence band absorption coefficient measurements in bulk layer, strained and unstrained multiquantum well 1.55 μm semiconductor lasers," *Electron. Lett.*, vol. 29, pp. 604–606, 1993.
[43] G. Fuchs, J. Hoerer, A. Hangleiter, V. Haerle, F. Scholz, R. W. Glew, and L. Goldstein, "Intervalence band absorption in strained and unstrained InGaAs multiple quantum well structures," *Appl. Phys. Lett.*, vol. 60, pp. 231–233, 1992.
[44] W. S. Ring, "Examinationof intervalence band absorption and its reduction by strain in 1.55μm compressively strained InGaAs/InP laser diodes," *Electron. Lett.*, vol. 30, pp. 306–308, 1994.
[45] T. Cho, H. Kim, Y. Kwon, and S. Hong, "Theoretical study on intervalence band absorption in InP-based quantum-well laser structures," *Appl. Phys. Lett. 68*, pp. 2183–2185, 1996.
[46] D. Regelman and D. Gershoni, private communication.
[47] P. Granestrand, K. Frojdh, O. Sahlen, B. Stoltz, and J. Walin, "Gain characteristics of QW lasers," in *Dig., Eur. Conf. Opt. Comm. ECOC*, 1998, pp. 431–432.
[48] P. Abraham, J. Piprek, and J. E. Bowers, "Improvement of internal quantum efficiency in 1.55μm laser diodes with InGaP electron stopper layer," *Jpn. J. Appl. Phys.*, pt. 1, vol. 38, pp. 90–93, 1999.
[49] R. F. Kazarinov and M. R. Pinto, "Carrier transport in laser heterostructures," *IEEE J. Quantum Electron.*, vol. 30, pp. 49–53, 1994.
[50] P. M. Smowton and P. Blood, "The differential efficiency of quantum well lasers," *IEEE J. Select. Topics Quantum Electron.*, vol. 3, pp. 491–498, 1997.
[51] G. J. Letal, J. G. Simmons, J. D. Evans, and G. P. Li, "Determination of active-region leakage currents in ridge-waveguide strained-layer quantum-well lasers by varying the ridge width," *IEEE J. Quantum Electron.*, vol. 34, pp. 512–518, 1998.

Joachim Piprek (M'94–SM'98) received the Ph.D. degree in solid-state physics from Humboldt University Berlin, Germany, in 1986.

He worked in industry and academia on the design and analysis of optoelectronic devices. He is currently an Adjunct Associate Professor at the University of California at Santa Barbara. His research interests include vertical-cavity lasers, novel semiconductor materials, and advanced computer simulation.

Patrick Abraham (M'99–SM'99) received the M.S. and Ph.D. degrees in material science from the University C. Bernard Lyon 1, France, in 1984, and 1987, respectively.

He was a Researcher at Centre National de la Recherche Scientifique (CNRS) and worked until 1988 for the Laboratoire de Physico-Chimie Minérale in France. He is currently a Research Engineer at the University of California at Santa Barbara, where his research interests include laser active region design, MOCVD growth, compliant substrates, and wafer fusing.

John E. Bowers (S'78–M'81–SM'85–F'93) received the Ph.D. degree in applied physics from Stanford University, Palo Alto, CA, in 1981.

He worked at Honeywell and AT&T Bell Laboratories before joining the University of California at Santa Barbara in 1987, where he is currently a Professor of Electrical Engineering, the Director of the Multidisciplinary Optical Switching Technology Center (MOST), and Member of the Heterogeneous Optoelectronics Technology Center (HOTC) and the NSF Center on Quantized Electronic Structures (QUEST). His main research interests are in the development of novel optoelectronic devices for the next generation of optical networks.